applied sciences

MDPI

*Article*

# Design and Dynamic Analysis of the Wire-Line Coring Robot for Deep Lunar Rocks

**Yufeng Wen [1], Guoqing Zhang [1,*], Heping Xie [2], Mingzhong Gao [2], Xu Zhang [1], Yaohui Wang [1] and Cunbao Li [2]**

[1] College of Mechatronics and Control Engineering, Shenzhen University, Shenzhen 518060, China
[2] Guangdong Provincial Key Laboratory of Deep Earth Sciences and Geothermal Energy Exploitation and Utilization, Institute of Deep Earth Sciences and Green Energy, College of Civil and Transportation Engineering, Shenzhen University, Shenzhen 518060, China
* Correspondence: zhanggq@szu.edu.cn; Tel.: +86-755-2653-6306; Fax: +86-755-2655-7471

**Abstract:** Deep lunar rocks carry geological information about the primitive Moon and are of great scientific value. In this paper, a coring robot for deep lunar rocks was proposed for the lunar environment based on the wire-line sampling device. This robot consists of the coring executor on the ground to assist in coring tube replacement and sample storage and the wireline self-excavating coring (WSC) robot for active drilling underground, which can provide autonomous deep coring on the moon. Subsequently, based on Prandtl's failure mechanism and the prediction equations of the mechanical properties of the lunar soil, the mathematical relationship between the ultimate support force and the depth of the support point of the WSC robot was constructed. Additionally, the drilling scheme of the WSC robot at different depths was also determined. The constraint model of the impact module was established, and the structural parameters were optimized through non-linear programming to achieve the maximum impact energy. Simulations of the impact process were then carried out in explicit dynamics. The simulation results show that the optimized impact module can effectively drill through the lunar rocks. This result validates, to some extent, the drilling capability of the WSC robot in lunar rocks. The research work can provide technical reference and theoretical support for deep coring lunar rocks.

**Keywords:** sampling device; impact mechanism; structure optimization; deep lunar rocks; wire-line sampling

check for updates

**Citation:** Wen, Y.; Zhang, G.; Xie, H.; Gao, M.; Zhang, X.; Wang, Y.; Li, C. Design and Dynamic Analysis of the Wire-Line Coring Robot for Deep Lunar Rocks. *Appl. Sci.* **2023**, *13*, 1722. https://doi.org/10.3390/app13031722

Academic Editor: Antonella Petrillo

Received: 23 December 2022
Revised: 19 January 2023
Accepted: 26 January 2023
Published: 29 January 2023



## 1. Introduction

Sampling for extraterrestrial subsurface exploration is an important tool for human understanding of the solar system and the universe, and it can help humans understand the formation process of celestial bodies [1]. In addition, sampling can effectively probe the precious metals and rare elements in celestial bodies, which can provide a good foundation for humans to utilize celestial bodies in the future [2]. Additionally, sampling can provide the necessary guarantee for the establishment of permanent interstellar bases [3]. The moon is the closest extraterrestrial object to the Earth, and it is the preferred target for the sampling of celestial bodies.

In the 1960s and 1970s, the Soviet Union and the United States carried out lunar exploration missions, namely the Luna program and the Apollo program [4]. There was also no lack of lunar surface sample return missions, such as the Apollo 17 mission. China also obtained lunar soil and returned it to Earth in 2020 [5]. Among the successful coring return missions, the Luna16 swing arm shallow drilling and the Chang'e-5 fixed drilling both achieved surface lunar soil coring [6]. the Apollo project used the astronaut-held Apollo lunar surface drill (ALSD) to achieve subsurface lunar soil coring up to 3.05 m [7]. To understand the celestial bodies more deeply, researchers now continue to develop deep sampling devices.

The current deep sampling devices for celestial bodies can be classified into two categories: multi-rod drilling sampling devices and wire-line sampling [8]. The multi-rod drilling sampling device is mature and stable. It is commonly loaded with multiple drilling rods and sampling tubes and achieves deep drilling by multiple combinations [9]. Therefore, institutions and researchers have built various devices to achieve deep sampling, such as the pneumatic multi-rod drilling device for lunar sampling [10], the Micro Robots for Scientific Applications 2 (RoSA2) [11], the Deep Drilling Rig (DeeDri) [12], and the Mars Astrobiology Research and Technology Experiment (MARTE) drilling system [13]. As a rule, the impact effect is applied by sampling devices in order to penetrate the deep hard layers more effectively [14]. However, in multi-rod drilling sampling devices, the energy lost due to thermal and rebound between drilling rods exceeds the energy used to destroy the terrain. Additionally, this phenomenon is further exacerbated by the increase in the number of connected segments in the sampling rod [15]. This makes multi-rod drilling sampling devices require more power and mass to achieve deep sampling.

The wire-line sampling device is connected to the lander by the power cable and drills deeper by its own self-excavation capability. It is more prone to jamming and requires higher soil properties at the sampling site than the multi-rod drilling sampling device. At the same time, it is difficult to drill in shallow and loose layers since a stable anchorage cannot be achieved in this layer [8]. However, the wire-line sampling device has the advantages of a compact structure, high energy utilization, low reaction force, and lightweight. These advantages provide obvious benefits for wire-line sampling devices for deep sampling. The wire-line sampling device is also considered the preferred option for sampling devices when drilling over a 10 m depth. The wire-line drilling device is softly connected to the surface by cables, which makes it necessary to drill itself through the self-excavation capability. The self-excavation capability of wire-line drilling devices can be accomplished in various approaches, including anchored drilling, bionic mole, bionic inchworm, etc. The bionic mole and bionic inchworm are able to propel at depth in the subsurface without lifting the drill. The feature of the bionic mole and the bionic inchworm leads to the increased usage of in situ probe emplacements, such as the mole carried by insight with the bionic mole [16] and the inchworm drilling (ID) System with the bionic inchworm [17]. However, the sampling missions, especially the full profile sampling, are accomplished by multiple liftings of the drill and collecting samples from each drill. For example, the Autonomous Tethered Corer achieved the drilling and coring of 10 m of limestone by multiple liftings of the drill and the removal of core samples. The coring device weighs 7 kg and has 50–75 W of power [18]; Auto-Gopher (AG) II with an ultrasonic percussion drill obtained a core at a 7.52 m depth with gypsum as the drilling target and is expected to achieve more than 50 m drilling [19]. However, the current wire-line sampling device still cannot achieve fully autonomous deep coring, and all the above drilling approaches require human assistance to exchange the coring tubes. Therefore, the development of a deep coring robot with autonomous capability is necessary.

In this paper, a wire-line robot for deep coring lunar rocks was designed with low energy consumption and a small space as an entry point. In addition, this robot provides a prototype solution for the deep coring of other celestial bodies. Firstly, the wire-line scheme was proposed, and the coring executor was designed. Secondly, a rotating impact composite coring robot with functions of subsurface anchoring, in-hole change in direction, etc., was designed for the requirements of subsurface self-excavation coring functions. Subsequently, the anchoring support force model with depth was established for the anchor module, which provided theoretical support for the drilling scheme at different depths. Finally, the structure parameters of the impact module were optimized with the objective of maximum impact energy. The optimized structure parameters were also simulated to verify the drilling and breaking effect of the impact module on the lunar rocks. The flow chart of the research methodology is shown in Figure 1.

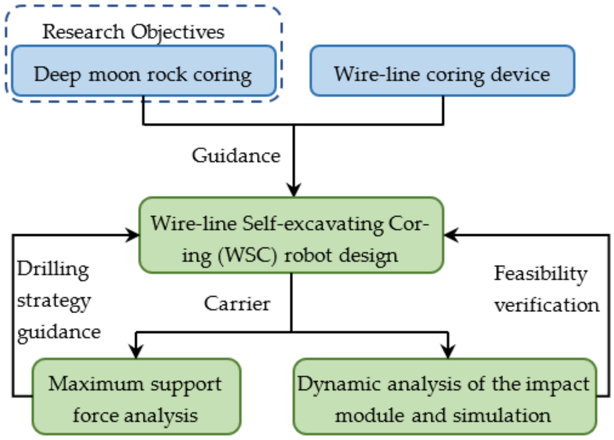


**Figure 1.** Methodological framework for the wire-line self-excavating coring robot research.

## 2. Design of the Wire-Line Coring Robot for Deep Lunar Rocks

With deep lunar rocks as the coring target, a wire-line coring robot incorporating a wire-line sampling device was proposed based on lightweight, low-power consumption design criteria and limited envelope space conditions. The wire-line coring robot can be divided into the coring executor and the wireline self-excavating coring (WSC) robot. The coring executor is responsible for replacing the coring tubes in the WSC robot and storing the core samples. The WSC robot is responsible for the underground autonomous drilling and coring work and is connected to the coring executor through an integrated cable.

### *2.1. Coring Executor*

The coring executor consists of the X-Z linear displacement robot, the fidelity chamber, etc., as shown in Figure 2. The X-Z linear displacement robot includes an X-axis displacement unit, Z-axis displacement unit, and clamping unit. The Z-axis displacement unit and the clamping unit are responsible for the coring tube replacement, while the X-axis displacement unit is combined with the C-axis rotation of the fidelity chamber to align the WSC robot with the storage hole. To identify the storage status of the coring tubes, the storage holes are numbered according to their positioning in the polar coordinate system, which consists of the C-axis and X-axis.

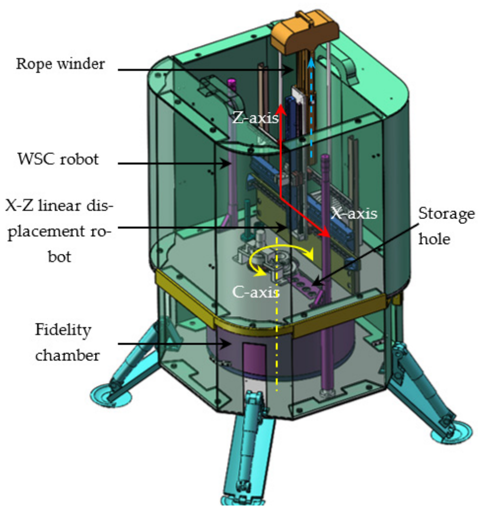


**Figure 2.** Design of the coring executor.

The coring executor coring process is as follows.

1. After the wire-line coring robot is placed on the moon, the exploding bolt works to separate the WSC robot from the coring executor, and the X-Z linear displacement

robot grabs the WSC robot and moves it to the center while loosening the cable of the rope winder;
2. The X-Z linear displacement robot releases the WSC robot, and then the rope winder slowly lifts the WSC robot down the through-hole by the cable. After dropping the specified amount of cable, the WSC robot begins coring work. When this coring phase is completed, the X-Z linear displacement robot grabs the WSC robot to fix the position;
3. The X-Z linear displacement robot and the fidelity chamber combine their movements to transport the WSC robot to the position corresponding to the number of this full coring tube. Then, the full coring tube is unloaded and installed into the empty coring tube by a Z-axis displacement unit. Repeat steps 2 and 3 until the desired mission target is completed.

### 2.2. Wire-Line Self-Excavating Coring Robot

The composition of the WSC robot is shown in Figure 3, including the pressure supply part, drilling part, and coring part. The pressure supply part fixes the WSC robot's position in the coring hole and provides drilling pressure. The drilling part provides rotational and impact functions to cut and break the lunar soil/rocks. The coring part stores the lunar soil/rocks coring samples and temporarily stores the debris generated in the coring. The WSC robot is modularly combined to realize the functions of each part. The modular design provides easy control of the size of the WSC robot and facilitates the functional testing of the prototype. The WSC robot is implemented mechanically with core actuators to reduce the energy supply burden, except for the modules that require an active drive.

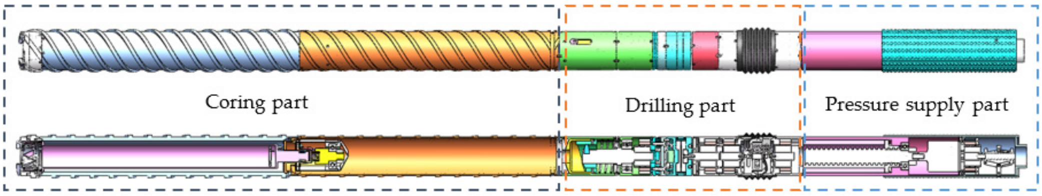


**Figure 3.** Design of the WSC robot.

The pressure supply part includes the anchor module which provides the support force in the hole, and the screw module to provide the drilling pressure, as is shown in Figure 4a. The anchor module is provided with three symmetrical crank slider mechanisms and anchor plates fixed on the sliders, where the crank is the same eccentric wheel. Therefore, the anchor plate can be driven by motors to synchronize the expansion, thus ensuring the positional anchoring of the WSC robot. To avoid anchor plate rebound during coring, a ratchet locking device is installed in the anchor module. The locking device is unlocked with the rope retrieval force so that the anchor plate can be retracted when the WSC robot is lifted. The locking device enables the anchor module to require less energy after deployment. Thus, the WSC robot can provide a higher energy supply for the drilling relative to other telescopic coring devices, such as the autonomous tethered corer.

The drilling part consists of the redirection module, the impact module, the rotation module, and a force sensor, as shown in Figure 5a. The redirection module has the ability to drive the WSC robot to shift direction actively in the hole so that the WSC robot can avoid extreme drilling situations, as shown in Figure 5b. The impact module generates the impact force through the spring energy storage mechanism. The application of the impact force can improve the drilling efficiency and reduce the torque for drilling the rocks. The force sensor is used to obtain real-time data on the axial force and rotational torque to make preliminary judgments on the current drilling situations.

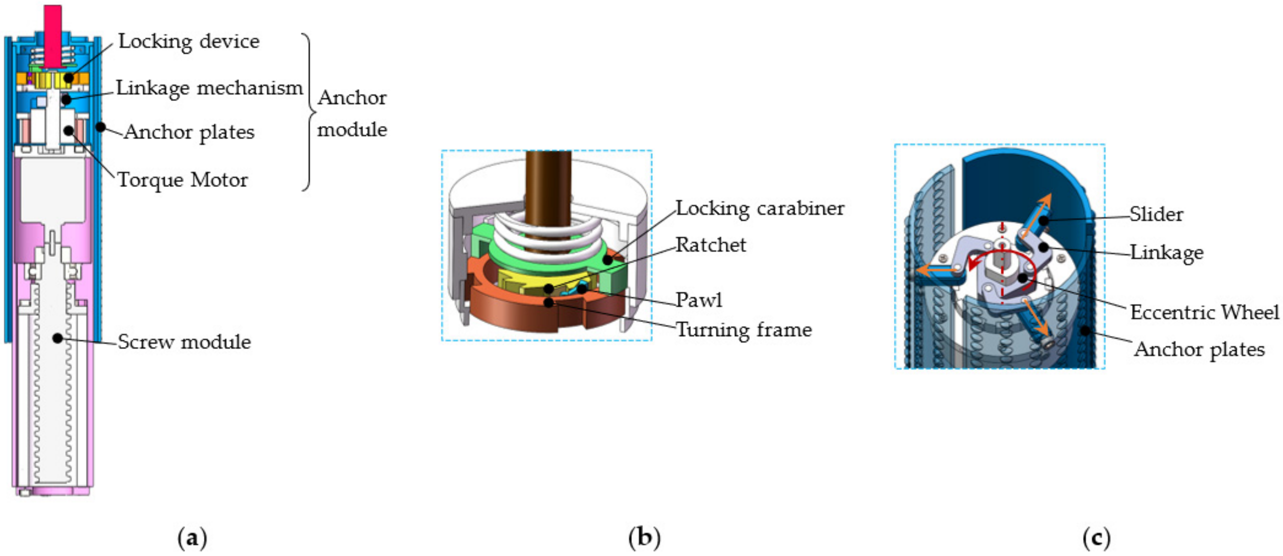


**Figure 4.** Design of the pressure supply part (**a**) Modules configuration (**b**) The locking device of the anchor module (**c**) Operation mechanism of the anchor module.

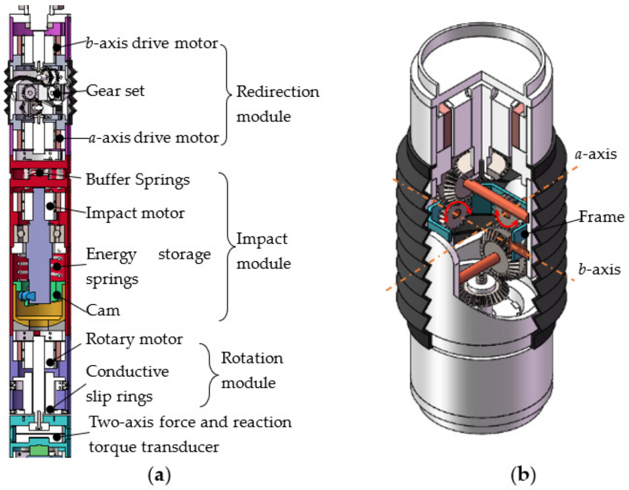


**Figure 5.** Design of the drilling part (**a**) Modules configuration (**b**) Operating mechanism of the redirection module.

The coring part can be divided into the debris-tolerant chamber, the connection module, the coring tube module, and the bit module, as shown in Figure 6. The coring part is a purely mechanical structure with the potential to be applied to other celestial bodies, such as Mars. Due to the load limitation of the aerospace mission, a consumable drilling fluid is not used to dispose of the debris that is generated during the coring process. Therefore, the debris-tolerant chamber is designed to temporarily store the debris. To dispose of the debris, the combination of the connection module and the debris-tolerant chamber enables the WSC robot to automatically discharge the debris after releasing the coring tube. Additionally, compared to other wire-line coring devices without waste chip handling, the setup of the debris-tolerant chamber significantly increases the length of the coring robot. However, debris increases the drilling resistance and leads to large amounts of debris in the subsequently collected samples. The connection module is designed with a heart-shaped slot and a spring, which enables the connection module to switch between the locked and unlocked states through a single application and unloading of the unidirectional Z-axis force. This state-switching function enables the WSC robot to replace coring tubes with unidirectional Z-axis forces ($F_z$), as shown in Figure 7. Meanwhile, the connection module is connected to other modules of the WSC robot through bearings, and this approach can avoid the interference of the rotational motion to the sample. The mechanically triggered truncation device is designed in the coring tube module for the composite lunar soil/rocks sampling requirement. This device uses a trigger plate to determine the position of the lunar soil/rocks in the coring tube, which triggers the truncator to cut and store the sample. Finally, to protect the drilling hole wall, the bit module can be transformed by the friction between the drilling tool and the drilling surface. The transformation capability of the bit module can shrink the drilling tool before lifting the WSC robot to reduce the scraping of the drilling tool and the drilling hole wall.

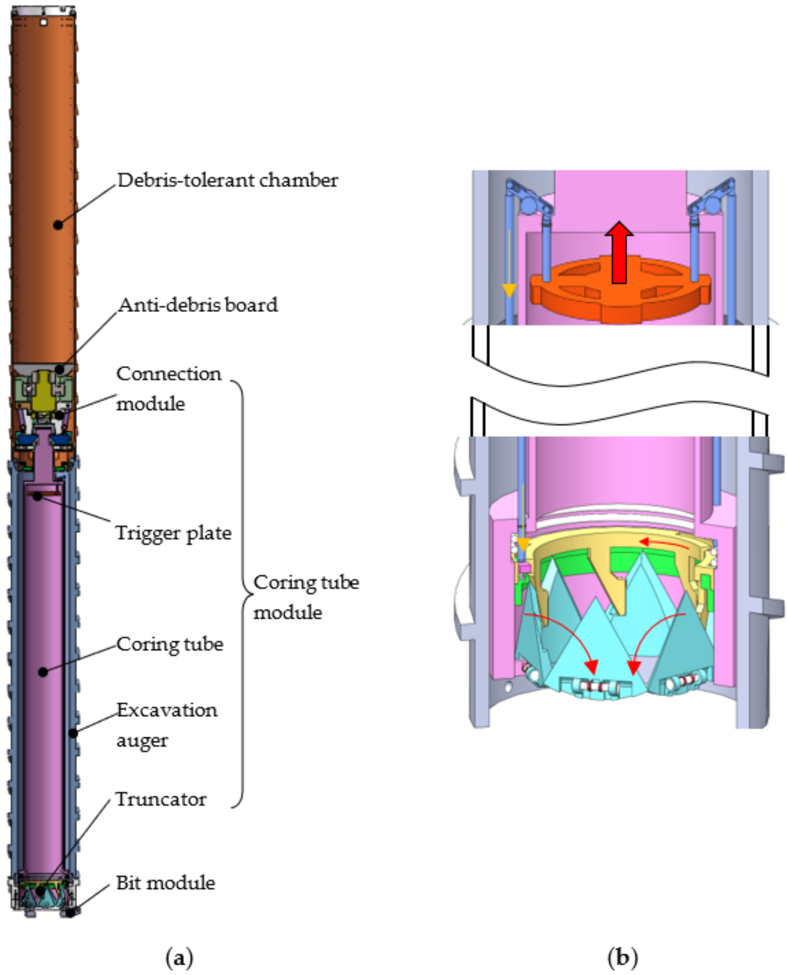


**Figure 6.** Design of the coring part (**a**) Modules configuration (**b**) Operating mechanism of truncator.

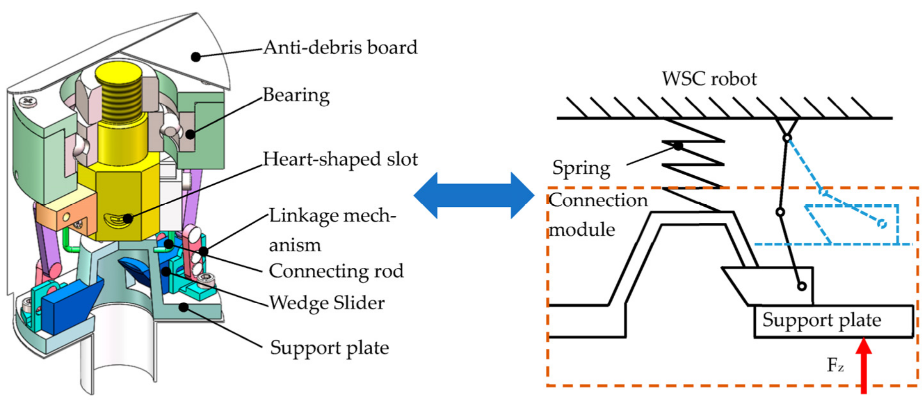


**Figure 7.** Design and operating mechanism of the connection module.

The single coring process of the WSC robot is as follows: after receiving the coring start signal from the coring executor, the anchor module is activated to anchor the WSC robot position. The screw module, rotation module, and impact module then work together to drill into the deep lunar rock. Finally, with the coring tube module automatically cut off and the storing of the lunar rock, the WSC robot is lifted back into the coring executor for coring tube replacement.

## 3. Dynamic Analysis of the WSC Robot

Part of the function modules in the WSC robot cannot be determined directly by the parameters of the original actuator, such as the anchor module and impact module. Therefore, the dynamic analysis of the impact module and the anchor module is targeted.

### 3.1. Maximum Support Force Analysis of the Anchor Module

The maximum support force is related to the drilling function of the WSC robot in the subsurface and is critical for the strategy of coring. The anchor module squeezes the drilling hole wall by expanding the anchor plates to provide sufficient friction to support the WSC robot underground. Thus, the higher the squeezing pressure, the stronger the support force of the WSC robot in the subsurface. However, the lunar regolith of the drilling hole wall can often slip when the squeeze pressure is excessive, thus preventing the anchor module from providing a stable positional fixation. Therefore, there is a limit to the support force provided by the anchor module.

For determining the maximum support force, the mechanical properties associated with the lunar regolith at different depths should be analyzed. According to NASA's analysis of the returned samples from the Apollo program, the relationship between the lunar regolith packing density $\rho$ and depth $z$ is [20]:

$$\rho = 1.92\frac{z+12.2}{z+18} \tag{1}$$

Additionally, the following relationship that exists between $\rho$ and the lunar regolith pore ratio $n$ is [21]:

$$n = 1 - \frac{\rho}{G\rho_w} \tag{2}$$

where $G$ is the average specific gravity of the lunar sample, with a suggested value of 3.1 [22] and $\rho_w$ is the density of pure water at 4 °C, which is 1 g/cm$^3$.

According to Prandtl's failure mechanism, the ultimate bearing capacity is related to cohesion and the angle of internal friction. Additionally, there is an exponential relationship between the lunar regolith pore ratio $n$ and the lunar regolith cohesion $c$, as well as a linear relationship with the tangent of the lunar regolith angle of the internal friction $\varphi$. Thus, the expressions for $c$ and $\varphi$ can be obtained by fitting the data from Table 1 [23]:

$$\begin{cases} c = 10^{2.9331-6.0035n} & \left(R^2 = 0.9885\right) \\ \varphi = \arctan(3.0982 - 4.1088n) & \left(R^2 = 0.9519\right) \end{cases} \tag{3}$$

**Table 1.** Estimated values of cohesion and the angle of internal friction of the lunar regolith at different depths (Data from reference [23]).

| Depths $z$ (m) | Cohesion $c$ (kPa) | Angle of Internal Friction $\varphi$ (°) |
|---|---|---|
| 0~0.15 | 0.44~0.62 | 41~43 |
| 0~0.3 | 0.74~1.1 | 44~47 |
| 0.3~0.6 | 2.4~3.8 | 52~55 |
| 0~0.6 | 1.3~1.9 | 48~51 |

Bringing Equations (1) and (2) into Equation (3) yields the expressions for $c$ and $\varphi$ with respect to $z$:

$$\begin{cases} c = 10^{2.93-\frac{3.69z+247.72}{z+18}} \\ \varphi = \arctan\left(3.1 - \frac{2.53z+169.54}{z+18}\right) \end{cases} \tag{4}$$

A schematic diagram of the slip surface of the anchoring area that was obtained according to Prandtl's failure mechanism is shown in Figure 8, in which Zone I is the active Rankine zone, Zone II is the Prandtl zone, and Zone III is the passive Rankine zone. According to Prandtl's theory, the ultimate bearing capacity of the hole wall can be obtained as:

$$p_u = cN_c + qdN_q \tag{5}$$

where $N_c = \cot\varphi\left[e^{\pi\tan\varphi}\tan^2\left(\frac{\pi}{4}+\frac{\varphi}{2}\right)-1\right]$, $N_q = e^{\pi\tan\varphi}\tan^2\left(\frac{\pi}{4}+\frac{\varphi}{2}\right)$, and $q$ is the uniform load in the passive Rankine zone, which can be considered as 0.

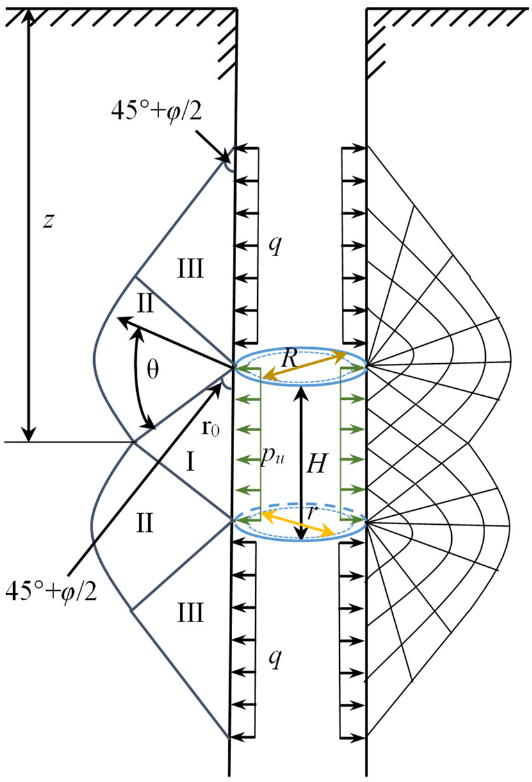


**Figure 8.** Schematic diagram of ultimate bearing capacity of drilling hole wall.

Since the anchor module is fixed in position by expanding the anchor plates, there are gaps after unfolding. Additionally, each anchor plate can still form a cylinder-like shape after the anchor module is unfolded. Therefore, the shape of the anchor module after unfolding is equated to an incomplete cylinder, and the missing part is represented by the equivalent rounded angle $\theta_m$ in the calculation, as follows:

$$\theta_m = 2\pi\frac{r}{R} \tag{6}$$

where $r$ is the radius of the anchor module when it is not unfolded, and $R$ is the length of the anchor plate unfolded from the center of the WSC robot.

Combining Equations (5) and (6) yields the maximum support force that the lunar regolith can withstand which is:

$$\frac{M_u}{R} + F_u \le \mu_s R H \theta_m p_u \tag{7}$$

where $\mu_s$ is the lunar regolith friction coefficient;

$H$ is the length of the anchor plate;

$M_u$ is the drilling torque;

$F_u$ is the drilling pressure.

If $H$ is determined, the relationship between the theoretical maximum drilling pressure and torque with depth can be obtained separately according to Equation (7), as shown in Figure 9. According to Figure 9, the drilling pressure and torque that can clearly be provided by the current depth support. Since the pore ratio of the shallow lunar regolith increases rapidly with the increase in lunar regolith depth, the anchoring effect in shallow lunar regolith above 0~4 m still varies drastically with the depth. The pore ratio of deep lunar regolith is close to the limit value, and the anchoring effect of the anchor module tends to be stable. Therefore, the drilling power needs to be changed in real-time when the WSC robot is working on shallow lunar regolith, and the full drilling power can be exerted when the WSC robot is working on a deep lunar regolith. According to the design target, the operation at full power is available in the lunar soil layer below 4.7 m depth. However, since the specific dynamic environment of the lunar soil layer is unknown, operation at full power should be performed again in deeper, more stable lunar soil below 7 m. When the anchor module was first anchored in the lunar soil, the bit module had already been drilled to a depth of more than 1 m. At this moment, the support force is hardly able to support the WSC robot to continue drilling. The solidifying cylinder could be added to assist with drilling.

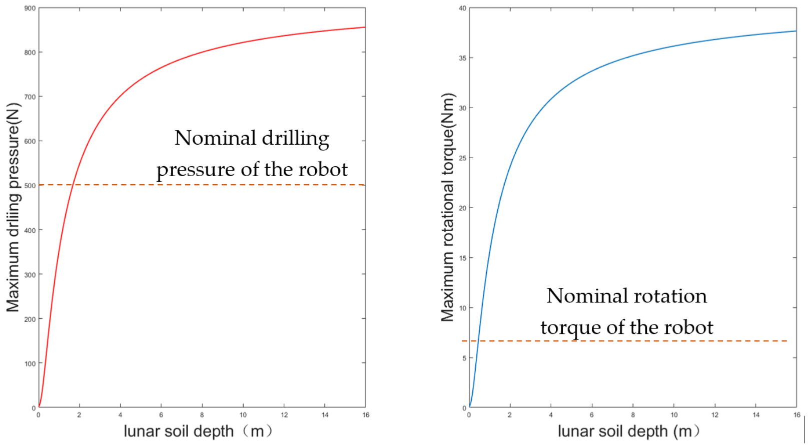


**Figure 9.** Maximum drilling pressure and rotational torque in relation to depth.

### *3.2. Dynamic Analysis of the Impact Module*

The impact module converts the kinetic energy of the motor rotation into impact energy by the spring energy storage mechanism. To analyze the dynamics of the impact module, the single impact process can be divided into the energy storage phase and the release phase. For the energy storage phase, the simplified cam curve can be expanded along a straight line, as shown in Figure 10, where the structural parameters are the cam radius $R_c$, spring preload length $l_0$, cam stroke height $h$, and drive wheel radius $R_d$. For the release phase, a certain length of the gentle section without loading is set on the cam to ensure the effective release of the impact energy and that the proportion of the loaded segment is $\alpha$. Among them, $\alpha$, $l_0$, and $h$ has a large impact on the impact work, so these parameters are used as optimization variables. For coil springs, based on the optimized design of cylindrical compression springs, the spring wire diameter $d$ and the effective number of turns $n$ are selected as optimization variables when the maximum energy storage in the restricted space is the optimization objective. The rest of the variables, such as the spring's mid-range $D$ and spring shear modulus $G_s$, are constants. Subsequently, the maximum impact energy as the objective function can be expressed as:

$$f(\mathbf{X}) = \frac{1}{2}kh(h+2l_0) + mg_{lunar}h + \frac{1}{2}m(\frac{\lambda h}{\alpha})^2 \tag{8}$$

where $k = \frac{G_s d^4}{8D^3 n}$ is the spring stiffness;
$g_{lunar}$ is the lunar gravitational acceleration;
$\lambda$ is the impact frequency;
$m$ is the mass of the impact hammer.
$\mathbf{X}$ = [$\alpha$ $l_0$ $h$ $d$ $n$].

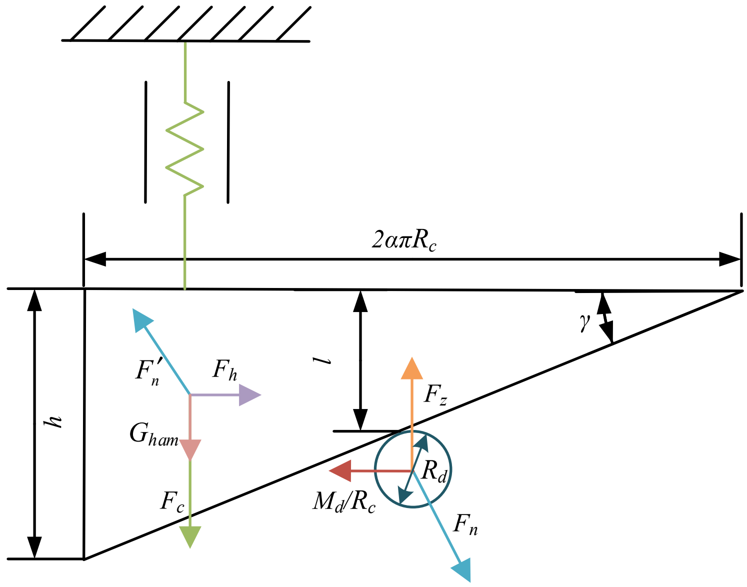


**Figure 10.** Simplified cam curve expanded along a straight line.

Based on spring design guidelines, the effect of the curvature factor $K$ should be considered when the spring is subjected to a dynamic load, which can be expressed as:

$$K = \frac{4C-1}{4C+4} + \frac{0.615}{C} \tag{9}$$

where $C = \frac{D}{d}$.

Based on the effect of the curvature factor, $d$ should satisfy the following constraints:

$$g_1 = \sqrt[3]{\frac{8KDF}{\pi[\tau]}} - d \leq 0 \tag{10}$$

The allowable shear stress $[\tau]$ decreases with the increase in the spring wire diameter; however, it is defined as a constant to simplify the optimization process. For installation space constraints, on the one hand, it is necessary to consider that the spring deformation needs to be smaller than the theoretical full deformation. On the other hand, it is necessary to consider that the height after pre-pressing is less than the installation space of the impact module $\mathrm{H}_0$. Accordingly, the installation dimensions are constrained as follows:

$$\begin{cases} g_2 = l_0 + h - \frac{D\pi n[\tau]}{KG_s d} \leq 0 \\ g_3 = \frac{D\pi n[\tau]}{KG_s d} + (n+1.5)d - h - \mathrm{H}_0 \leq 0 \end{cases} \tag{11}$$

For the energy storage phase, an analysis of Figure 10 yields the constrained relationship between the motor torque and the structure parameters during cam energy storage.

$$g_4 = [G_{ham} + k(l_0 + l)]\frac{h}{2\pi\alpha} - M_d \leq 0 \tag{12}$$

where $M_d$ is the nominal torque of the motor;

$l$ is the current axial displacement of the roller, with the maximum value of $h$;

$G_{ham}$ is the gravity of the impact hammer.

For the release phase, if the friction between the impact hammer and the guide wall is neglected, the equation of state for the release phase of the impact hammer is:

$$\ddot{l} = -\left(g_{lunar} + \frac{k(l_0 + l)}{m}\right) \tag{13}$$

The analysis of the motion of the impact hammer provides the following initial conditions for the motion of the impact hammer at the cam notch:

$$\begin{cases} l(0) = h \\ \dot{l}(0) = \frac{\lambda h}{\alpha} \\ \ddot{l}(0) = -\left(g_{lunar} + \frac{k(l_0+h)}{m}\right) \end{cases} \tag{14}$$

Substituting the initial conditions into Equation (13) for the solution yields the time from the release of the impact hammer to the return of the initial height as:

$$t_1 = \sqrt{\frac{m}{k}}\left[\arcsin\left(\frac{mg + kl_0}{k\sqrt{a^2 + b^2}}\right) - \arccos\left(\frac{b}{\sqrt{a^2 + b^2}}\right)\right] \tag{15}$$

where $a = \frac{mg_{lunar}}{k} + l_0 + h$,

$b = \frac{\sqrt{\frac{m}{k}}\lambda h}{\alpha}$.

Assuming that the impact energy takes time to be fully released and it is set to $t_2$, the constraint that ensures that the impact energy is fully released before loading is:

$$g_5 = 2\pi R_c \lambda (t_1 + t_2) + 2R_d - 2\pi R_c(1 - \alpha) \leq 0 \tag{16}$$

According to Equations (8), (10)–(12), (16), and the inherent boundaries of each parameter, the numerical model of the constraint problem can be obtained as:

$$\begin{aligned} &\max f(\mathbf{X}) = \tfrac{1}{2}kh(h + 2l_0) + mg_{lunar}h + \tfrac{1}{2}m\left(\tfrac{\lambda h}{\alpha}\right)^2 \\ &s.t.\ \ g_1 = \sqrt[3]{\tfrac{8KDF}{\pi[\tau]}} - d \leq 0 \\ &\qquad g_2 = l_0 + h - \tfrac{D\pi n[\tau]}{KG_s d} \leq 0 \\ &\qquad g_3 = \tfrac{D\pi n[\tau]}{KG_s d} + (n + 1.5)d - h - \mathrm{H}_0 \leq 0 \\ &\qquad g_4 = [G_{ham} + k(l_0 + l)]\tfrac{h}{2\pi\alpha} - M_d \leq 0 \\ &\qquad g_5 = 2\pi R_c\lambda(t_1 + t_2) + 2R_d - 2\pi R_c(1 - \alpha) \leq 0 \\ &\qquad g_6 = \alpha - 1 \leq 0 \\ &\qquad g_7 = -\alpha \leq 0 \\ &\qquad g_8 = -l_0 \leq 0 \\ &\qquad g_9 = -h \leq 0 \\ &\qquad g_{10} = h - 50 \leq 0 \\ &\qquad g_{11} = 0.05 - d \leq 0 \\ &\qquad g_{12} = d - 1.5 \leq 0 \\ &\qquad g_{13} = 1.5 - n \leq 0 \\ &\qquad g_{14} = n - 200 \leq 0 \end{aligned} \tag{17}$$

Since the length of the WSC robot was limited by the mission objectives, the working space reserved for the impact module was only 20 mm after the necessary equipment was designed. Additionally, the available installation diameter of the WSC robot was only 38 mm. Considering the working space and working environment of the WSC robot, the parameters were initially determined as follows: the nominal torque and rotation rate of the impact motor were 0.84 Nm and 600 rpm; the energy storage spring was made of oil-quenched and annealed spring steel wire with a shear modulus of 78.5 GPa and tensile strength of 1540 MPa; the mass of the impact hammer was predicted to be 190 g based on its 3D model; $t_2$ was set to 1 ms. If the energy consumption during impact loading, such as friction, is neglected, the global optimal solution of Equation (17) can be obtained by combining the optimization toolbox with the global optimization algorithm in MATLAB. The optimization results after rounding are shown in Table 2. The optimized theoretical single maximum impact energy can reach 3.7 J.

**Table 2.** Structural parameters of the optimized impact module.

| Motor Torque $M_d$ (Nm) | Cam Stroke Height $h$ (mm) | Preload Length $l_0$ (mm) | Spring Stiffness $k$ (N/m) | Proportion of the Loaded Segment $\alpha$ (%) | Impact Mass $M$ (g) | Impact Frequency $\lambda$ (Hz) |
|---|---|---|---|---|---|---|
| 0.84 | 8.75 | 5.75 | 40,000 | 95 | 190 | 10 |

The finite element simulation of the impact process on lunar rocks was carried out in LS-DYNA with optimized structural parameters to verify the performance of the impact module. The lunar rocks model used the modified HJC constitutive model in LS-DYNA, and the parameter settings are shown in Table 3. Both the coring tube and the impact hammer use pre-defined isotropic elastic models of aluminum alloy and steel, respectively.

**Table 3.** HJC constitutive parameters of lunar rocks (Data from reference [24,25]).

| Density $\rho$ (kg/m$^3$) | Shear Modulus G (GPa) | Tensile Strength T (MPa) | Uniaxial Compressive Strength $f_c$ (MPa) | Cohesive Strength A | Pressure Hardening B | Strain Rate Coefficient C | Pressure Hardening Exponent N |
|---|---|---|---|---|---|---|---|
| 2164 | 4.437 | 1.107 | 70.27 | 0.79 | 1.6 | 0.007 | 0.61 |

The impact stress wave generated by the impact hammer is transmitted to the lunar rocks through the coring tube, and the stress wave transmission simulation effect is shown in Figure 11. The bit module is driven by the impact action to intrude into the lunar rocks and form an impact crushing pit at the contact point. At the same time, the lunar rocks around the bit module generate stress concentration in a short period of time, which leads to cracks inside. During the simulation, the impact stress wave is loaded to the lunar rocks at 0.16 ms, which causes the lunar rock to produce a crushing pit, as shown in Figure 12a. By this time, part of the impact energy in the coring tube has been consumed; however, another part of the impact energy still exists in the coring tube in the form of reflected stress waves. The reflected stress waves are repeatedly returned in the coring tube to enlarge the impact-crushing pit. During the simulation, the drill bit intrudes into the moon rock at a 1.2 mm depth after the initial impact loading and eventually to a 4.3 mm depth. However, the reflected stress wave in the actual experiment is usually consumed greatly during the reflection process, and the final intrusion depth does not surpass the initial intrusion depth too much.

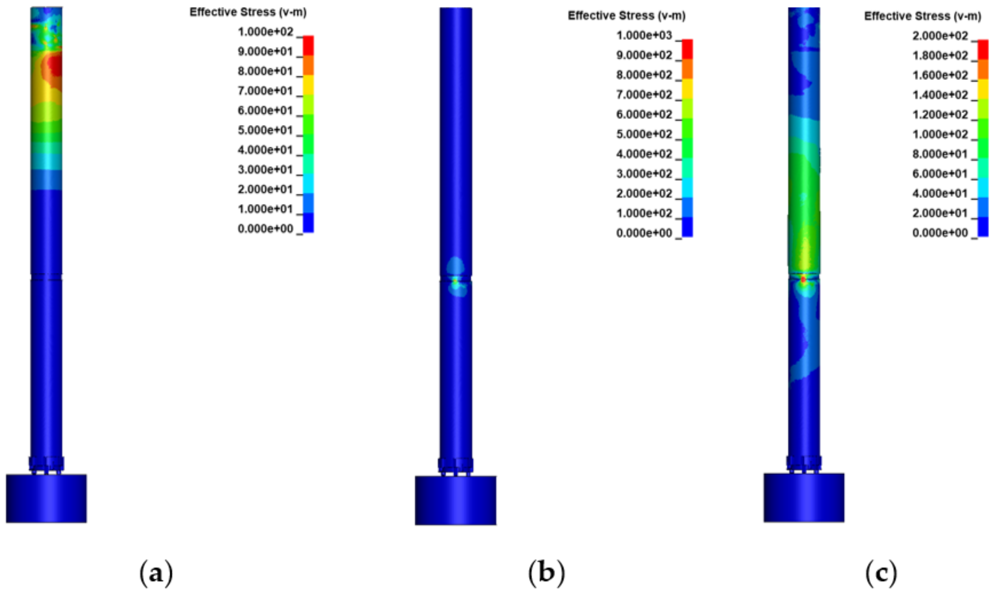


**Figure 11.** Stress waves during intrusion of lunar rocks by the WSC robot (**a**) Load phase (**b**) Transfer to connection point (**c**) Reflection phase.

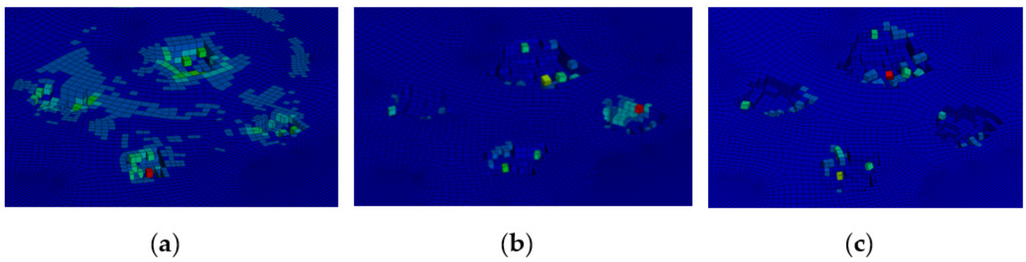


**Figure 12.** Lunar rocks crushing simulation results (**a**) 0.16 ms; (**b**) 1 ms; (**c**) 2 ms.

## 4. Conclusions

This paper designs a coring robot for deep lunar rocks based on a wire-line sampling device: the WSC robot. The WSC robot has functions, such as a subsurface anchor module and debris-tolerant chamber, which makes it possible to complete the whole coring process in the subsurface autonomously. The coring executor has the functions of changing the coring tubes and storing full sample coring tubes. Then, the dynamic analysis of the anchor module in the WSC robot can be carried out. A lunar regolith greater than 4 m is tight enough to support the full-power WSC robot according to the model of support force versus the depth of the lunar regolith in this paper. The support force provided by the lunar regolith at 0–4 m varies considerably with depth, and the support condition needs to be monitored in real-time to change the WSC robot power output. Finally, the impact function of the WSC robot is modeled and optimized, and the maximum impact energy based on the spring storage mechanism is determined to be 3.7 J. Then, this impact process is simulated, and it is determined that the WSC robot could effectively produce impact-crushing pits on the lunar rocks. Thus, the rock drilling capability of the WSC robot is initially verified, and the basis for the prototype is provided.

**Author Contributions:** Y.W. (Yufeng Wen) and G.Z. completed the main research tasks and wrote the manuscript. G.Z. revised the whole manuscript. H.X. proposed the initial ideas. M.G. and C.L. completed the derivation of the theory related to the soil mechanics. X.Z. and Y.W. (Yaohui Wang) assisted in the design of the mechanical structure. All authors have read and agreed to the published version of the manuscript.

**Funding:** The work described in this paper was supported by the National Natural Science Foundation of China (Grant Nos. U2013603, 52275454, 51827901), and the Shenzhen Natural Science Foundation (Grant Nos. 20200826160002001, JCYJ20220531103614032).

**Institutional Review Board Statement:** Not applicable.

**Data Availability Statement:** Not applicable.

**Conflicts of Interest:** The authors declare no conflict of interest.

## References

1. Zhang, T.; Xu, K.; Yao, Z.X.; Ding, X.L.; Zhao, Z.; Hou, X.Y.; Pang, Y.; Lai, X.M.; Zhang, W.M.; Liu, S.T.; et al. The progress of extraterrestrial regolith-sampling robots. *Nat. Astron.* **2019**, *3*, 487–497. [CrossRef]
2. Bar-Cohen, Y.; Zacny, K. *Drilling in Extreme Environments: Penetration and Sampling on Earth and other Planets*; Wiley-VCH: Berlin, Germany, 2009.
3. Badescu, V.; Zacny, K. *Inner Solar System: Prospective Energy and Material Resources*; Springer: Cham, Switzerland, 2015. [CrossRef]
4. Zhang, T.; Wang, B.; Wei, H.; Zhang, Y.; Chao, C.; Xu, K.; Ding, X.; Hou, X.; Zhao, Z. Review on planetary regolith-sampling technology. *Prog. Aeronaut. Sci.* **2021**, *127*, 1–26. [CrossRef]
5. Qiao, L.; Chen, J.; Xu, L.; Wan, S.; Cao, H.; Li, B.; Ling, Z. Geology of the Chang'e-5 landing site: Constraints on the sources of samples returned from a young nearside mare. *Icarus* **2021**, *364*, 114480. [CrossRef]
6. Slyuta, E. Chapter 3—The Luna program. In *Sample Return Missions*; Longobardo, A., Ed.; Elsevier: Amsterdam, The Netherlands, 2021; pp. 37–78. [CrossRef]
7. Jerde, E.A. Chapter 2—The Apollo program. In *Sample Return Missions*; Longobardo, A., Ed.; Elsevier: Amsterdam, The Netherlands, 2021; pp. 9–36. [CrossRef]
8. Zhang, X.; Zhang, G.Q.; Xie, H.P.; Gao, M.Z.; Wen, Y.F. A Review of Sampling Exploration and Devices for Extraterrestrial Celestial Bodies. *Space Sci. Rev.* **2022**, *218*, 1–50. [CrossRef]
9. Zhang, Y.L.; Zhang, T.; Wei, H.Y.; Liu, J.B.; Wang, W.; Yuan, X.Y.; Pang, Y.; Guan, Y.S.; Hou, X.Y.; Xu, K. Advances in Extraterrestrial Drilling Technology to Discover the Secrets Hidden Inside Celestial Bodies. *Space Sci. Rev.* **2022**, *218*, 1–46. [CrossRef]
10. Liang, P.; Hou, X.; Zhang, K.; Zhang, K.; Deng, Z. The research and design of pneumatic multi-pipe deep lunar soil drilling device. In Proceedings of the 2016 IEEE International Conference on Mechatronics and Automation, Harbin, China, 7–10 August 2016; pp. 1379–1384. [CrossRef]
11. Bogatcbev, A.; Koutcberenko, V.; Malenkov, M.; Matrossov, S. Developments of Track Locomotion Systems for Planetary Mobile Robots. *IFAC Proc. Vol.* **2004**, *37*, 153–158. [CrossRef]
12. Magnani, P.G.; Re, E.; Ylikorpi, T.; Cherubini, G.; Olivieri, A. Deep drill (DeeDri) for Mars application. *Planet. Space Sci.* **2004**, *52*, 79–82. [CrossRef]
13. Cannon, H.N.; Stoker, C.R.; Dunagan, S.E.; Davis, K.; Gómez-Elvira, J.; Glass, B.J.; Lemke, L.G.; Miller, D.; Bonaccorsi, R.; Branson, M.; et al. MARTE: Technology development and lessons learned from a Mars drilling mission simulation. *J. Field Robot.* **2007**, *24*, 877–905. [CrossRef]
14. Li, P.; Zhang, H.; Jiang, S.Y.; Zhang, W.W. Analysis and Testing of Load Characteristics for Rotary-Percussive Drilling of Lunar Rock Simulant with a Lunar Regolith Coring Bit. *Shock. Vib.* **2017**, *2017*, 3012749. [CrossRef]
15. Szwarc, T.J. Thermal Modeling of Coring and Drilling Operations for Solar System Exploration Applications. Ph.D. Thesis, Stanford University, Stanford, CA, USA, 2013.
16. Marshall, J.P.; Hudson, T.L.; Andrade, J.E. Experimental Investigation of InSight HP3 Mole Interaction with Martian Regolith Simulant. *Space Sci. Rev.* **2017**, *211*, 239–258. [CrossRef]
17. Zhang, W.; Li, L.; Jiang, S.; Ji, J.; Deng, Z. Inchworm Drilling System for Planetary Subsurface Exploration. *IEEE/ASME Trans. Mechatron.* **2020**, *25*, 837–847. [CrossRef]
18. Zacny, K.; Bar-Cohen, Y.; Brennan, M.; Briggs, G.; Cooper, G.; Davis, K.; Dolgin, B.; Glaser, D.; Glass, B.; Gorevan, S.; et al. Drilling systems for extraterrestrial subsurface exploration. *Astrobiology* **2008**, *8*, 665–706. [CrossRef] [PubMed]
19. Bar-Cohen, Y.; Zacny, K.; Badescu, M.; Lee, H.J.; Sherrit, S.; Bao, X.Q.; Freeman, D.; Paulsen, G.L.; Beegle, L. Auto-Gopher-2-Wireline Deep Sampler Driven by Percussive Piezoelectric Actuator and Rotary EM Motors. *Adv. Sci. Technol.* **2016**, *100*, 207–212.
20. Heiken, G.H.; Vaniman, D.T.; French, B.M. *Lunar Sourcebook, A User's Guide to the Moon*; Press Syndicate of the University of Cambridge: New York, NY, USA, 1991.
21. Mitchell, J.K.; Houston, W.N.; Carrier, W.; Costes, N.C. Apollo soil mechanics experiment S-200. *Arch. Dermatol. Syphilol.* **1974**, *53*, 19740019219.
22. Duke, M.; Woo, C.; Sellers, G.; Bird, M.; Finkelman, R. Genesis of lunar soil at Tranquillity Base. In Proceedings of the The Apollo 11 Lunar Science Conference, Houston, TX, USA, 1 January 1970; pp. 347–361.
23. Mitchell, J.; Houston, W.; Scott, R.; Costes, N.; Carrier III, W.; Bromwell, L. Mechanical properties of lunar soil: Density, porosity, cohesion and angle of internal friction. In Proceedings of the The Third Lunar Science Conference, Houston, TX, USA, 1 January 1972; pp. 3235–3253.

24. Pham, K.D.; Zhao, W.; Zmuda, H.; Sun, H.; Jia, Q.; Cox, J.L.; Meyer, G.J.; Zhang, Y. Mechanical analysis about the spherical mobile robot on the moon environment. In *Sensors and Systems for Space Applications IV*; SPIE: Orlando, FL, USA, 2011. [CrossRef]
25. Yang, Z. *Research on Impact Crushing in Luna Soil Sampling Based on ANSYS/Ls-Dyna Numerical Simulation Master*; Harbin Institute of Technology Harbin: Harbin, China, 2019.